Fracture Strength and Toughness of Ultra High-Strength TRIP-aided Steels

Koh-ichi Sugimoto

Department of Mechanical Systems Engineering, Shinshu University, 4-17-1, Wakasato, Nagano 380-8553, Japan.

E-mail: sugimot@shinshu-u.ac.jp

Phone: +81-26-269-5114; Fax: +81-26-269-5109

Abstract

The performance of hydrogen embrittlement, fatigue properties and impact toughness of ultra high-strength TRIP-aided steels with bainitic ferrite matrix (TBF steels) has been discussed. Some characteristics and deformation-transformation mechanism of the retained austenite has also been discussed. It has been observed that mechanical stability and volume fraction of the interlath retained austenite phase in the TBF steels play an important role in increasing delayed fracture strength, fatigue limit and impact toughness.

Introduction

In order to obtain an extreme weight reduction and crash worthiness performance of automobiles, high formable and ultra high-strength sheet steels with tensile strength of 780-1470 MPa are required for automotive parts such as center pillar reinforcement, seat frame and so on. Transformation-induced plasticity (TRIP) [1] of retained austenite is very useful for improving the formability of these steels. On the basis of such an idea, 0.15-0.40%C-Si-Mn high-strength steel containing metastable retained austenite, "TRIP-aided steel with polygonal ferrite matrix (TPF)", has been developed by the addition of about 1.5 mass% Si to low carbon steel and austempering after annealing [2-11], as shown in **Figure 1a**.

Fig.1

Fortunately, the TPF steel is attained extremely large total elongation of 30-40% due to the strain-induced transformation in a large strain range. However, the stretch-flangeability has been improved only a little, compared to dual-phase steel [12,13] (**Figure 2a**). The tensile strength of this steel could not exceed 980 MPa, because the matrix structure is based on soft polygonal ferrite due to intercritical annealing. Furthermore, galvanizing and galvanealing are difficult because insoluble silicon oxide layer is formed due to the addition of Si and only a small amount of retained austenite is left at austempering temperature corresponding to hot-dip galvanizing and galvannealing temperatures (460°C and 520°C, respectively).

Fig.2

These weak points corresponding to the formability may be overcome by the following means or techniques which change the morphology and stability of retained austenite:

(a) replacement of matrix structure [4,12-18] improving the formability (particularly stretch-flangeability) and increasing the strength,

(b) warm forming [4,6,7,12,13] enhancing the formability,

(c) microalloying [9,16-30] suppressing to form silicon oxide, raising the optimum austempering temperature for galvanizing and galvanealing, and improving the formability

If the matrix structure is changed by annealed martensite structure (**Figure 1(b)** and **(d)**), the best combination of stretch-formability and stretch-flangeability can be attained in the steel (TAM steel) [15], as shown in **Figure 2**. On the other hand, when matrix structure is replaced with bainitic ferrite (**Figure 1(c)** and **(e)**), martensite or these combined structure has ability to enhance the yield stress and tensile strength of the steel (TBF steel) to 980-1470 MPa by maintaining a good stretch-flangeability (**Figure 2**). Even though when hold or martempered at temperatures lower than martensite-start temperature, good stretch-flangeability of the TBF steel can be achieved [14,17,18]. It is noteworthy that microstructure of this TBF steel is resemble to steel subjected to quenching and partitioning (Q&P) process proposed by Speer et al. [31].

In this paper, hydrogen embrittlement performance, fatigue properties and impact toughness of the ultra high-strength TBF steels has been introduced by our research group.

Carbon enrichment mechanism and strain-induced transformation of retained austenite

TBF steel is produced by hot rolling or annealing after cold rolling, followed by austempering in a bainite transformation temperature range (**Figure 3a**). The carbon Fig.3

concentration of retained austenite is progressed to T_0 or T_0' line during austempering after hot rolling or annealing [32], if cementite precipitation is suppressed by the addition of Si, Al etc. (**Figure 3b**). The volume fraction of retained austenite (f_{γ}) is quantified from integrated intensity of (200)α, (211)α, (200)γ, (220)γ and (311)γ peaks of Mo-Kα radiation, as given by the following equation [33].

$$f_{\gamma} = \frac{1}{\left[Z\left(\frac{P_{\alpha}}{P_{\gamma}} \right) + 1 \right]} \quad (1)$$

where P_{α} and P_{γ} are the X-ray diffraction intensities of α and γ diffraction planes, respectively. Z is constant given by the combination of α and γ diffraction planes.

The carbon concentration (C_{γ}, mass%) has been estimated by substituting the lattice constant (a_{γ}, 10^{-1} nm) measured from (200)γ, (220)γ and (311)γ peaks of Cu-Kα radiation into the following equation [34].

$$a_{\gamma} = 3.5780 + 0.0330 \text{ x } (\%C_{\gamma}) + 0.00095 \text{ x } (\%Mn_{\gamma}) - 0.0002 \text{ x } (\%Ni_{\gamma}) + 0.0006 \text{ x } (\%Cr_{\gamma}) + 0.0220 \text{ x } (\%N_{\gamma}) + 0.0056 \text{ x } (\%Al_{\gamma}) - 0.0004 \text{ x } (\%Co_{\gamma}) + 0.0015 \text{ x } (\%Cu_{\gamma}) + 0.0031 \text{ x } (\%Mo_{\gamma}) + 0.0051 \text{ x } (\%Nb_{\gamma}) + 0.0039 \text{ x } (\%Ti_{\gamma}) + 0.0018 \text{ x } (\%V_{\gamma}) + 0.0018 \text{ x } (\%W_{\gamma}) \quad (2)$$

where $\%Mn_{\gamma}$, $\%Ni_{\gamma}$, $\%Cr_{\gamma}$, $\%N_{\gamma}$, $\%Al_{\gamma}$, $\%Co_{\gamma}$, $\%Cu_{\gamma}$, $\%Mo_{\gamma}$, $\%Nb_{\gamma}$, $\%Ti_{\gamma}$, $\%V_{\gamma}$ and $\%W_{\gamma}$ represent the solute contents (mass%) of the individual alloying elements in retained austenite. For the convenience, they have been assumed to be equivalent to the added contents.

Retained austenite stability against straining, "*mechanical stability*", is controlled by carbon concentration, morphology and size of retained austenite phase, strength of matrix

structure, stress state, temperature and strain rate, etc. For the transformation-induced plasticity of low alloy TRIP-aided steels, the following three temperature ranges are of importance (**Figures 4** [35] and **5** [23]).

Fig.4

Fig.5

(a) $\boldsymbol{M_S - M_S^{\sigma}}$ **range:**

At M_S^{σ}, the stress needed to initiate the martensitic transformation of the retained austenite equals the yield strength of the parent γ phase. Below this temperature, the retained austenite transforms to martensite via preexisting nucleation sites. As the temperature increases, the stress needed for the martensitic transformation also increases since the chemical driving force decreases.

(b) $\boldsymbol{M_S^{\sigma} - M_d}$ **range:**

Above the M_S^{σ} temperature, the austenite is strained. The martensite is now predominantly nucleated at new nucleation sites produced by slip. Note that this martensite is not of the high carbon plate type and will not have the brittleness associated with the plate type martensite. Yielding of the austenite is by glide. The transformation is mainly strain-induced. Additional nucleation occurs at the intersection of strain-induced deformation bands.

(c) $\boldsymbol{T > M_d}$**:**

The M_d temperature is the temperature above which no martensite transformation occurs. The higher temperature results in a higher stacking fault energy and a lower driving force for transformation; no transformation occurs as a result of straining.

If the mechanical stability of the retained austenite is defined by the following k value [6,7,12,36], typical forming temperature dependence of the k value is shown in **Figure 6**. Fig.6

$$\ln f_{\gamma 0} - \ln f_{\gamma} = k\,\varepsilon \tag{3}$$

where f_{γ} and $f_{\gamma 0}$ are volume fraction of retained austenite after strained to ε and initial one, respectively. The k value becomes the minimum at about T_S=100-150°C [7,12,36]. The strain-induced martensite transformation (SIMT) preferentially takes place below the T_S (**Figure 6b**). On the other hand, strain-induced bainite transformation preferentially occurs above the T_S. The lower the strain rate, the higher the k-value [7]. It is of importance that equi-biaxial deformation raises the k-value, compared to uniaxial deformation [8,36]. In true TRIP steels such as Fe-Cr-Ni [1,39] and Fe-Ni-C [39] metastable austenitic stainless steels, the k value becomes zero above M_d temperature.

Bhadeshia et al. [37] has rewritten the equation (3) as follows,

$$\ln f_{\gamma 0} / f_{\gamma} = k_1\,\Delta G^{\alpha'\gamma}\varepsilon \tag{4}$$

where $\Delta G^{\alpha'\gamma}$ is the chemical free energy change ($\Delta G^{\alpha'\gamma} = \Delta G^{\gamma} - \Delta G^{\alpha'}$) for the transformation of austenite to ferrite of the same composition (without considering stored energy due to the shape deformation) and k_1 is the material constant. After straining, the carbon concentration of retained austenite increases because the retained austenite with lower carbon concentration is preferentially transformed to martensite [38].

Retained austenite characteristics

Conventional TRIP-aided steel (TPF steel) has blocky or granular types of retained austenite phase. Since the inter particle path is relatively large, high carbon concentration can not be attained, especially in high austempering temperature corresponding to hot-dip galvanizing. Imai et al. [21] stabilized the unstable retained austenite by Al addition because Al raises T_0 (T_0') temperature and suppresses cementite reaction. In TAM and TBF steels, the retained austenite morphology changes to needle-like and filmy types, respectively. In addition, matrix structures of these steels are characterized by annealed martensite and bainitic ferrite lath structures, respectively, which possess different dislocation density (**Figure 1(d)** and **(e)**). Due to which the small inter particle path of retained austenite is attained in the TAM and TBF steels.

When retained austenite characteristics are compared in three kinds of TRIP-aided steels with different matrix structure, TAM steel is characterized by higher volume fraction and carbon concentration of retained austenite (**Figure 7**). On the other hand, the volume fraction of retained austenite of TBF steel is nearly the same or slightly decreases compared to that of TPF steel, although its carbon concentration is as high as TAM steel. The carbon concentrations of TAM and TBF steels are nearly agree with T_0 line (**Figure 3b**) where ferrite and austenite of the same chemical composition have identical chemical free energy. Hence, this agrees with the result of those steels do not contain any cementites.

Fig.7

In general, optimum austempering holding time (t_A) of TAM and TBF steels are shorter than TPF steel, despite of the higher carbon concentration of retained austenite [15]. In addition, the carbon concentration at retained austenite/matrix interface is enriched [21]. When the

structure of matrix is lath type, the interfacial area increases. Hence, the high mean carbon concentration of the TAM and TBF steels is considered as a result from the fine lath structure matrix and small interparticle path, as shown in **Figure 8**. Fig.8

According to Aaronson [40], the annealed martensite lath structure is maintained for group I (Fe-C-Mn, Fe-C-Ni, Fe-C-Cu) and group II (Fe-C-Si, Fe-C-Al, Fe-C-Co) because the alloying elements of groups I and II promote the nucleation of austenite along the lath boundary of martensite which forms during intercritical annealing. So, it is impossible to makes an ideal annealed martensite lath structure for group III (Fe-C, Fe-C-Mo, Fe-C-Cr) steels.

Deformation mechanism

According to the previous study [41], the deformation of TRIP-aided steels is principally controlled by the following two items:

(a) Increase in strain-induced martensite content and stress relaxation (or plastic relaxation) due to shear strain and expansion strain on the strain-induced transformation to martensite.

(b) Compressive internal stress in the matrix resulting from strain-hardened retained austenite and other hard second phases.

When the items (a) and (b) are applied to the deformation theory of two phase alloy [42], an increment of strain-hardening ($\Delta\sigma_h$) has been obtained due to the second phase from the following equation [41] (as shown in **Figure 9**). Fig.9

$$\Delta\sigma_h(\varepsilon) = \sigma(\varepsilon) - \sigma^M(\varepsilon) = \sigma_i(\varepsilon) + \sigma_t(\varepsilon) + \sigma_f(\varepsilon) \quad (5)$$

where ε is a plastic-strain, σ and σ^M represent flow stresses of the TRIP-aided steel and the matrix, respectively and σ_i, σ_t and σ_f are the "*mean internal stress*" (or long-range internal stress), "*strain-induced martensite hardening*" [41] and "*forest-hardening*" proposed by Ashby [43], respectively. They have been proposed as follow:

$$\sigma_i(\varepsilon) = \{(7-5\nu)\mu/5(1-\nu)\} \cdot f \cdot \varepsilon_P^u \quad (6)$$

$$\sigma_t(\varepsilon) = g\,(f_{\alpha m}^*) \quad (7)$$

$$\sigma_f(\varepsilon) = \zeta\mu(\mathbf{b} \cdot f \cdot \varepsilon/2r)^{1/2} \quad (8)$$

where υ and μ are the Poisson's ratio and the shear modulus of each phase, respectively. ε_P^u is the "*eigen strain*" [44], f is the volume fraction of the second phase, and $g(f_{\alpha m}^*)$ is obtained as a function of the volume fraction of strain-induced martensite content $f_{\alpha m}^*$. The term ζ is a constant, **b** is the Burgers vector and r denotes the mean diameter of the second phase particles.

In TBF steel, contribution of the mean internal stress is relatively small, and most of strain hardening results from strain-induced martensite hardening. When TRIP-aided steels are deformed at about 150°C, the total elongation considerably increases, accompanied with decreased flow stress because retained austenite effectively transforms to martensite at a large strain range [36,45], especially when Al and other alloying elements are added into the steel. Mukherjee et al. [46] have reported that total elongation of 980MPa grade Al-Nb-Mo bearing TPF steel (0.4%C-0.5%Si-1.5%Mn-1.0%Al-0.05%Nb-0.2%Mo) increases to 78% by deformation at 150°C and strain rate of $3.3\text{x}10^{-3}$/s, although it is about 20% at 20°C testing.

It is noteworthy that the combination of tensile strength and elongation is the same level as that of Fe-Mn-Al-Si TWIP steel [47]. It has been reported in the literature [48] that very high internal stress develops in the matrix of TPF steel with only a small amount of strain-induced transformation if the steel is strained at 150°C. So, extreme large total elongation at 150°C of the TPF steel may be associated with stabilization of retained austenite (effective strain-induced transformation in a large strain range) and the resultant high long range internal stress due to difference in flow stress between soft matrix and hard retained austenite.

Hydrogen embrittlement

In general, hydrogen embrittlement performance is important for automotive body design when tensile strength of the steel is above 1200 MPa. Hojo et al. [49-52] investigated the delayed fracture strength of 0.2%C-0.5-1.5%Si-1.5%Mn-0.04-1.0%Al TBF steels with tensile strength above 1200 MPa. **Figure 10** shows typical micrographs of these TBF steels austempered below M_S. **Figure 11** shows delayed fracture limit (DFL) for 5 hours of these TBF steels. The 0.2%C-1.5%Si-1.5%Mn TBF steel (base steel) exhibits higher delayed fracture strength than martensitic steel. If Al of 0.2-0.5mass% is added to the base TBF steel with removal of the same amount of Si, the TBF steels possess extremely high delayed fracture strength. These delayed fracture limits are decreased by prestraining, but the decreased amount is lesser than that of martensitic steel [52].

Fig.10

Fig.11

The effects of microalloying (Nb, Mo and Mn) have also been examined for delayed fracture limit. In result, only Mn considerably deteriorates the delayed fracture strength [52]. From SEM observation, it is found that intergranular fracture occurs in 2.5% Mn bearing steel

(**Figure 12**). On the other hand, quasi-cleavage fracture is appeared on fracture surface of base steel and Al bearing steels, without intergranular fracture. Fig.12

According to Tsubakino et al. [53] and Gu et al. [54], most of the hydrogen is trapped in retained austenite or at retained austenite/matrix interface, as well as at fine carbide interface, on dislocation and on grain boundary. It has been reported in the literature [51] that when diffusible hydrogen of TBF steel is measured, the hydrogen evolution rate increases at 100-150°C **(Figure 13**). So, the above mentioned high delayed fracture limit of TBF base steel may be associated with the presence of retained austenite phase. Namely, retained austenite traps most of the hydrogen and disturbs the diffusion to prior austenite grain boundary, resulting suppress the grain boundary fracture. It has been expected that further high delayed fracture limit obtained in Al bearing TBF steel is due to enrichment of carbon in stable retained austenite [52] because it suppresses the stress-assisted transformation to martensite (**Figure 14**) and also suppress the hydrogen discharge into prior austenitic grain boundary. Fig.13 Fig.14

Fatigue properties

If low alloy TRIP-aided steel is applied to automotive suspension parts, high fatigue limit and cyclic hardening are required. **Figure 15** [55] shows cyclic hardening behavior of 0.17%C-1.41%Si-2.02%Mn TPF and TBF steels. Differing from conventional high strength precipitation hardening steel, TPF and TBF steels exhibit a significant cyclic hardening, in the same way as dual-phase (DP) steel. According to Sugimoto et al. [41,55], the large cyclic hardening of TPF and TBF steels is associated with a high long range internal stress and the strain-induced transformation hardening of retained austenite. Contribution of the internal stress to the total Fig.15

amount of cyclic hardening is relatively large in TPF steel due to a large difference in flow stress between matrix and second phase [41,55]. Even after forming to 5-10% strain, the above cyclic hardening appears in the TPF and TBF steels [41].

Figure 16 [56] shows fatigue limit of three kinds of TRIP-aided steels with the same chemical composition of 0.17%C, 1.41%Si and 2.00%Mn before and after prestraining. These TRIP-aided steels represent higher fatigue limits than dual-phase (DP) steel. After prestraining, the fatigue strength further increases due to the increased yield stress, particularly in TPF steel. This is considered to be due to the increased internal stress. The increased fatigue limit of TPF steel has also been reported by Yokoi [57]. Furthermore, Cheng et al. has been reported that retained austenite suppresses crack propagation [58]. Fig.16

Figure 17 [59] shows the variations in fatigue limit as a function of austempering temperature in 0.2-0.4%C-1.5%Si-1.5%Mn TBF steels. When TBF steel is austempered at temperatures below M_S, the fatigue limit (FL) decreases although the yields stress (YS) and tensile strength (TS) increase so much. Thus, these FL/TS ratios possess low values. Note that these fatigue limits have a linear relation with proportional limit, not yield stress and tensile strength. This fact indicates that high mobile dislocation density of matrix results in low fatigue limit of smooth specimen. Fig.17

Figure 18 [59] shows notch sensitivity index ($q=(K_f-1)/(K_t-1)$, K_f: fatigue-notch factor, K_t: stress concentration factor) [60] of 0.2%C-1.5%Si-1.5%Mn TBF steel (steel A) and 0.2%C-1.0%C-1.5%Mn-0.5%Al-0.05%Nb-0.2%Mo TBF steel (steel B) austempered at 425^{o}C for 200s. These TBF steels represent lower notch sensitivity of fatigue limit than martensitic steel (steel C). Fig.18

It is noteworthy that the steel B possesses the lowest notch sensitivity. The steel B is characterized by high carbon concentration (high mechanical stability) of retained austenite due to Al addition and refined grain size due to Nb addition. In addition, fatigue crack mainly propagated zigzag along lath boundary. So, it is considered that the high stability of retained austenite of steel B effectively suppresses crack initiation and/or propagation through plastic relaxation by the strain-induced transformation [59], as well as a small interlath distance of retained austenite and refined matrix structure, especially for notched specimens.

Impact toughness

Impact members of vehicles require high impact absorbed performance. It has been reported in the literature [61] that TPF steel possesses a superior impact performance compared to that of precipitation hardening and banitic steels and similar to dual-phase steel. It may be due to the strain-induced transformation of retained austenite which improves the impact performance, which is in agreement with the previous finding [61].

Song et al. [62] carried out Charpy impact tests of 0.11%C-1.3%Si-1.0%Mn (Ms= 471°C) and 0.20%C-2.0%Si-1.5%Mn (Ms=419°C) TBF steels to measure impact absorbed value (CIAV) and fracture appearance transition temperature (FATT). Resultantly, they found that TBF steels achieved high upper shelf values and low transition temperatures (**Figures 19** and **20**). If the TBF steels are austempered at temperatures lower than M_S temperature, these impact characteristics are further improved, compared to dual-phase steel and TPF steel. Also, the TBF steels possess lower FATT than the TPF steel.

Fig.19

Fig.20

According to Knott [63], if the plastic zone (d_Y) of cleavage or quasi-cleavage crack is expressed as the following equation, the d_Y values of the TBF and TFP steels are calculated as 5-10μm and 3μm, respectively.

$$d_Y = K^2/3\pi\sigma_Y^2 \quad (9)$$

where K and σ_Y are stress intensity factor and yield stress, respectively. Since mean free path of retained austenite phase in the steels are 1-2μm and 5μm, respectively, the plastic zone of the TBF steel includes a large amount of retained austenite films, differing from that of the TFP steel (as shown in **Figure 21**). So, the refined inter particle path of retained austenite films in the TBF steel is considered to effectively suppress the propagation of cleavage crack, in the same way as the initiation of cleavage crack, as well as the stabilized (carbon-enriched) retained austenite. Bhadeshia and Edmonds [64] has also been reported that retained austenite plays an important role of suppressing void and crack initiation through plastic relaxation of stress concentration due to the strain-induced transformation.

Fig.21

When the TBF steel is ausformed, followed by austempering at temperatures lower than *M*s, the Charpy impact absorbed value significantly increases with increase in both the tensile strength and total elongation [65]. This is due to (i) refining of microstructure (matrix and retained austenite structure) by dynamic and static recrystalization on ausforming and (ii) the volume fraction of retained austenite increases, although the carbon concentration of retained austenite decreases.

Summary

In this paper, hydrogen embrittlement performance, fatigue properties and impact toughness of ultra high-strength TBF steel has been introduced and related with the characteristics of retained austenite.

(1) Delayed fracture strength of the TBF steel increases vastly compared to that of martensitic steel, especially when 0.2-1.0%Al is added. This is due to the following reasons:

(a) stress-assisted martensite transformation of retained austenite is suppressed due to stabilized or carbon-enriched retained austenite.
(b) intergranular fracture is suppressed by that hydrogen are preferentially trapped in retained austenite.
(c) strain-induced transformation of the retained austenite relaxed the localized stress concentration to suppress the crack and/or void initiation.

(2) The TBF steel exhibits significant cyclic hardening due to the strain-induced transformation hardening and a long range internal stress hardening. Fatigue limit of the TBF steel has a linear relationship with proportional limit, not yield stress and tensile strength. In addition, the steel has been achieved higher notched fatigue performance or lower notch-sensitivity than conventional martensitic steel, due to TRIP effect of retained austenite. Complex additions of 0.5%Al, 0.05%Nb and 0.2%Mo considerably improved the notched fatigue performance, as well as the smooth fatigue strength. This is associated with the stabilized retained austenite and refined microstructure, suppressing

fatigue crack initiation and/or propagation.

(3) The TBF steel has been achieved high upper shelf value and low transition temperature. The high impact performance is due to the refining of inter particle path of retained austenite and stabilized (carbon-enriched) retained austenite. In this case, the retained austenite plays an important role of suppressing void and crack initiation through plastic relaxation of stress concentration due to the strain-induced transformation.

References

1. F. Zackay, E. R. Parker, D. Fahr and R. Busch: Trans. Amer. Soc. Metal, 1967, **60**, 252-259.
2. O. Matsumura, Y. Sakuma and H. Takechi: Trans. Iron Steel Inst. Jpn., 1987, **27**, 570-579.
3. H. C. Chen, H. Era and M. Shimizu: Metall. Trans. A, 1989, **20A**, 437-445.
4. K. Sugimoto, M. Misu, M. Kobayashi and H. Shirasawa: ISIJ Int., 1993, **33**, 775-782.
5. Y. Sakuma, O. Matsumura and H. Takechi; Metall. Trans. A, 1991, **22A**, 489-498.
6. K. Sugimoto, N. Usui, M. Kobayashi and S. Hashimoto: ISIJ Int., 1992, **32**, 1311-1318.
7. K. Sugimoto, M. Kobayashi and S. Hashimoto: Metall. Trans. A, 1992, **23A**, 3085-3091.
8. S. Hiwatashi, M. Takahashi, T. Katayama and M. Usuda: J. Jpn. Soc. Technol. Plast., 1994, **35**, 1109-1114.
9. Z. Hanzaki, P. D. Hodgson and S. Yue: ISIJ Int., 1995, **35**, 79-85.
10. Jacqes, E. Girault, P. Harlet, and F. Delannay: ISIJ Int., 2001, **41**, 1061-1067.
11. B. C. De Cooman, Proc. of International Conference on TRIP-Aided High Strength Ferrous Alloys, ed. by B. C. DeCooman, GRIPS' Sparkling World of Steel, Belgium, 2002

12. K. Sugimoto, A. Nagasaka and M. Kobayashi: Proc. Inter. Sympo. on Hot Workability of Steels and Light Alloys-Composites, CIM, Montreal, 1996, 503-514.
13. K. Sugimoto: Trans. Indian Inst. Met., 2006, **59**, 725-738.
14. K. Sugimoto, J. Sakaguchi, T. Iida and T. Kashima, ISIJ Int., 2000, **40**, 920-926.
15. K. Sugimoto, A. Kanda, R. Kikuchi, S. Hashimoto, T. Kashima and S. Ikeda: ISIJ Int., 2002, **42**, 910-915.
16. K. Sugimoto, B. Yu, Y. Mukai and S. Ikeda: ISIJ Int., 2005, **45**, 1194-1200.
17. K. Sugimoto, K. Nakano, S. Song and T. Kashima: ISIJ Int., 2002, **42**, 450-455.
18. K. Sugimoto, M. Murata, T. Muramatsu and Y. Mukai: ISIJ Int., 2007, **47**, 1357-1362.
19. K. Hulka, W. Bleck and K. Papamantellos: 41st MWSP Conf. Proc., ISS, 1999, **37**, 67-77.
20. S. Hashimoto, S. Ikeda, K. Sugimoto and S. Miyake: ISIJ Int., 2004, **44**, 1590-1598.
21. N. Imai, N. Komatsubara and K. Kunishige: CAMP-ISIJ, 1995, **8**, 572-575.
22. L. Barbe, L. T. Martinez, B. C. DeCooman: Proc. of Int. Conf. on TRIP-Aided High Strength Ferrous Alloys, ed. by B. C. DeCooman, GRIPS' Sparkling World of Steel, Belgium, 2002, 147-151.
23. B. C. DeCooman: Solid State Mater. Sci., **2004, 8**, 285-303.
24. S. Traint, A. Pichler, M. Blaimschein, B. Röthler, C. Krempaszky and E. Werner: Proc. Int. Conference on Advanced High Strength Sheet Steels for Automotive Applications, AIST, PA, 2004, 79-98.
25. E. Girault, A. Mertens, P. Jacqes, Y. Houbaert, B. Verlinden and J. V. Humbeeck: Scripta Materialia, 2001, **44**, 885-892.
26. J. Ohlert, W. Bleck and K. Hulka: Proc. of International Conference on TRIP-Aided High Strength Ferrous Alloys, GRIPS' Sparkling World of Steel, Belgium, 2002, 199-206.

27. S. Jiao, F. Hassani, R. L. Donaberger, E. Essadiqi and S. Yue: ISIJ International, 2002, **42**, 299-303.

28. I. B. Timokhina, E. V. Pereloma and P. D. Hodgson: Proc. of Int. Symp. on Transformation and Deformation Mechanism in Advanced High-Strength Steels, MetSoc&CIM, BC, Canada, 2003, 331-344.

29. A. K. Srivastava, D. Bhattachrjee, G Jha, N. Gope and S. B. Singh: Mat. Sci. and Eng. A, 2007, **445**–**446**, 549–557.

30. A. K. De, R. S. Kircher, J. G. Speer and D. K. Matlock: Proc. Int. Conference on Advanced High Strength Sheet Steels for Automotive Applications, AIST, PA, 2004, 337-348.

31. A. M. Streicher, J. G. Speer, D. K. Matlock and B. C. DeCooman: Int. Conf. on Advanced High Strength Sheet Steels for Automotive Applications Proc., AIST, PA, 2004, 51-62.

32. M. Takahashi and H.K.D. Bhadeshia: Mater. Trans, JIM, 1991, **32**, 689-696.

33. H. Maruyama: J. Jpn. Soc. Heat Treat., 1977, **17**, 198-204.

34. D. J. Dyson and B. Holmes: J. Iron Steel Inst., 1970, **208**, 469-474.

35. M. Azuma, N. Fujita, M. Takahashi, T. Iung, O. Bouaziz, M. Goune, A. Perlade and D. Quidort: Int. Conf. on Advanced High Strength Sheet Steels for Automotive Applications Proc., AIST, PA, 2004, 269-276.

36. K. Sugimoto, M. Kobayashi, A. Nagasaka and S. Hashimoto: ISIJ Int., 1995, **35**, 1407-1414.

37. M. Y. Sherif, Mateo C. Garcia, T. Sourmail and H. K. D. H. Bhadeshia: Mat. Sci. and Technol., 2004, **20**, 319-321.

38. A. Itami, M. Takahashi and K. Ushioda: Proc. of the Sympo. on High-Strength Sheet Steels for the Automotive Industry, ed. by Pradhan, ISS, Warrendale, PA, 1994, 245-254.

39. I. Tamura, T. Maki and H. Hato: Trans. Iron Steel Inst. Jpn., **10** (1970) 163.40. M. R. Plichta and H. I. Aaronson: Metall. Trans., 1974, **5**, 2611-2613.

41. K. Sugimoto, M. Kobayashi and S. Yasuki: Metall. Trans. A, 1997, **28A**, 2637-2643.

42. Y. W. Chang and R. J. Asaro: Metal Sci., 1978, **12**, 277-284.

43. M. F. Ashby: Philos. Mag., 1966, **14**, 1157-1178.

44. T. Mura and T. Mori: Micromechanics, Baifukan, Tokyo, 1976, 23.

45. L. Samek L, E. DeMoor and B. C. DeCooman: Int. Conf. on Advanced High Strength Sheet Steels for Automotive Applications Proc., AIST, PA, 2004, 361.

46. M. Mukherjee, O. N. Mohanty, S. Hashimoto, T. Hojo and K. Sugimoto: ISIJ Int., 2006, **46**, 316-324.

47. U. Brux, G. Frommeyer, O. Grassel, L. W. Meyer and A. Weise: Steel Research, 2002, **73**, 294-299.

48. K. Sugimoto, M. Kobayashi, H. Matsushima and S. Hashimoto: Trans. Jpn. Soc. Mech. Eng. A, 1995, **16A**, 80-86.

49. T. Hojo, S. Song, K. Sugimoto, A. Nagasaka, S. Ikeda, H. Akamizu and M. Mayuzumi: Tetsu-to-Hagane, 2004, **90**, 177-182.

50. T. Hojo, K. Sugimoto, Y. Mukai and S. Ikeda: Second Int. Conf. on Advanced Structural Steels (ICASS2004), CSM, China, 2004, 638-641.

51. T. Hojo, K. Sugimoto, Y. Mukai, H. Akamizu and S. Ikeda: Tetsu-to-Hagane, 2006, **92**, 83-89.

52. T. Hojo T, K. Sugimoto, Y. Mukai and S. Ikeda; Tetsu-to-Hagane, 2007, **93**, 234-239.

53. H. Tsubakino and H. Harada; Advances in Delayed Fracture Solution, ISIJ, Tokyo, 1977, 138-143.

54. J. L. Gu, K. D. Chang, H. S. Fang and B. Z. Bai: ISIJ Int., 2002, **42**, 1560-1564.

55. K. Sugimoto, S. Song, K. Inoue, M. Kobayashi and S. Masuda: J. Soc. Mater. Sci. Jpn, 2001, **50**, 657-664.

56. S. Song, K. Sugimoto, S. Kandaka, A. Futamura, M. Kobayashi and S. Masuda: Mater. Sci. Res. Int., 2003, **9**, 223-229.

57. T. Yokoi, M. Takahashi and N. Ikenaga: SAE Technical Paper 2001-01-0042, 2002.

58. X. Cheng, R. Petrov, L. Zhao and M. Janssen: Engineering Fracture Mechanics, 2008, **75**, 739-749.

59. K. Sugimoto, J. Tsuruta and S. Song: Key Eng. Mater., 2007, **345-346**, 247-250.

60. G. E. Dieter, Mechanical Metallurgy, SI Metric Edition, McGraw-Hill Book Company, Singapore, 1988, 403.

61. M. Takahashi: Nippon Steel Technical Report, 2003, **88**, 2-7.

62. S. Song, K. Sugimoto, M. Kobayashi, H. Matsubara and H. Kashima: *Tetsu-to-Hagane*, 2000, **86**, 563-569.

63. J. F. Knott: Fundamentals of Fracture Mechanics, Bifukan , Tokyo, Japan, 1977, 138.

64. H. K. D. H. Bhadeshia and D. V. Edmonds: *Met. Sci.*, 1983, **17**, 411-419.

65. K. Sugimoto, M. Ito, S. Hashimoto and S. Ikeda: .Mat. Sci. Forum, 2007, **539-543**, 4309-4314.

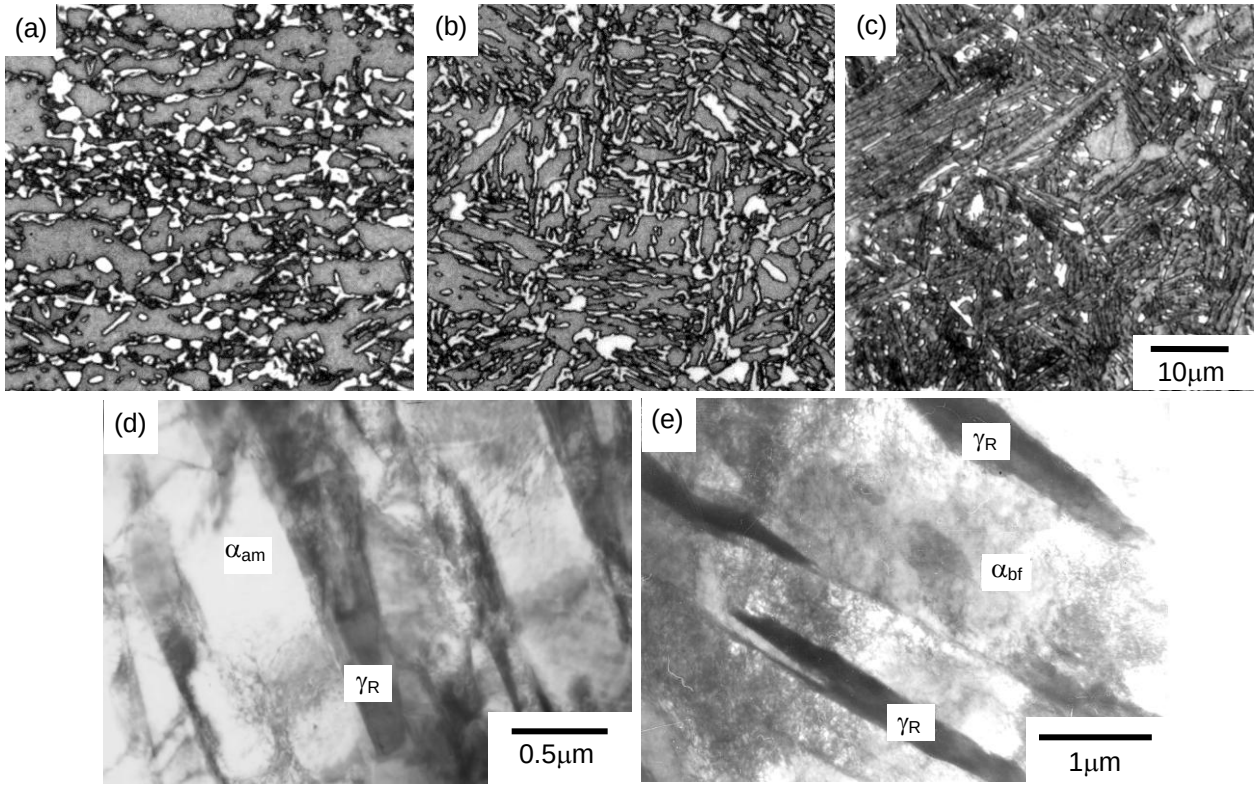

Figure 1: Typical light micrographs (a-c) and transmission electron micrographs (d, e) of (a) 0.2%C-1.5%Si-1.5%Mn TPF (t_A=1000s), (b, d) TAM (t_A=100s) and (c, e) TBF (t_A=200s) steels austempered at 400^{o}C. In (a)-(c), gray, black and white regions represent matrix ((a) polygonal ferrite, (b) annealed martensite; α_{am}, (c) bainitic ferrite; α_{bf}), cementite-free bainite and retained austenite (γ_R) and/or martensite, respectively.

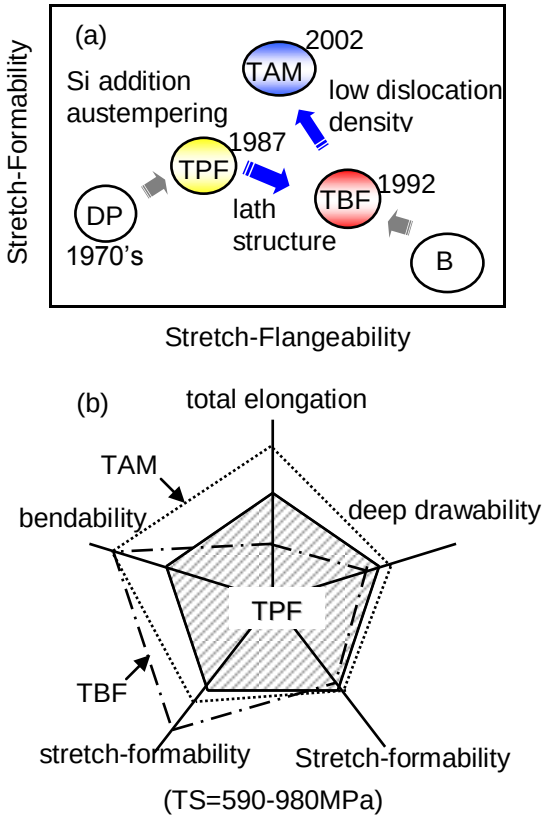

Figure 2: Development history and comparison of some formabilities of three kinds of low alloy TRIP-aided steels with different matrix structure, polygonal ferrite (TPF), bainitic ferrite (TBF) or annealed martensite (TAM), in which DP and B steels are dual-phase and bainitic steels, respectively.

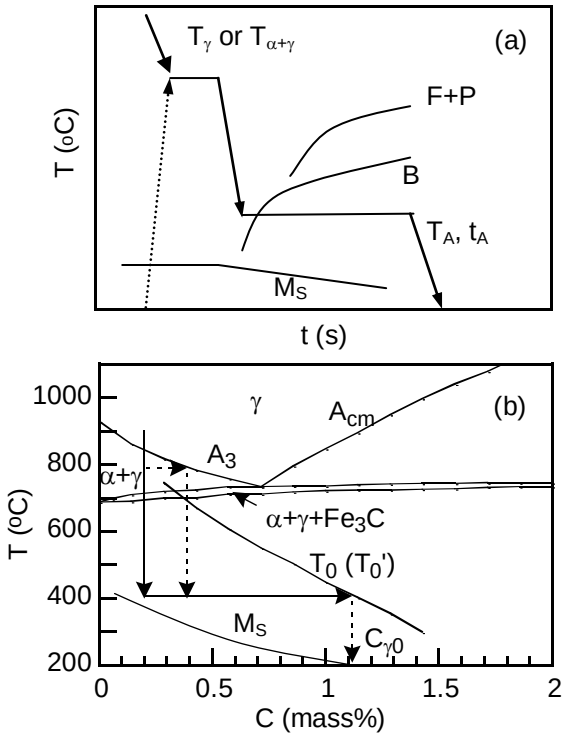

Figure 3: Annealing-austempering process and pseudo-binary Fe-C-1.5Si-1.5%Mn diagram, in which T_γ and $T_{\alpha+\gamma}$ represent annealing temperatures in γ and $\alpha+\gamma$ regions, respectively. T_A and t_A are austempering temperature and time, respectively.

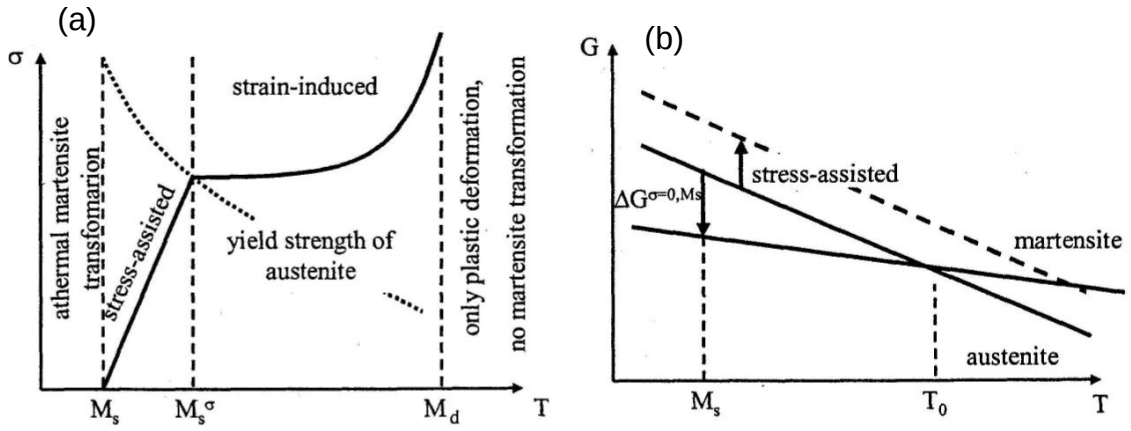

Figure 4: Relationship between stress-assisted and strain-induced martensite [35]. $\Delta G^{\sigma=0,\ Ms}$ is energy for transformation of austenite to martensite.

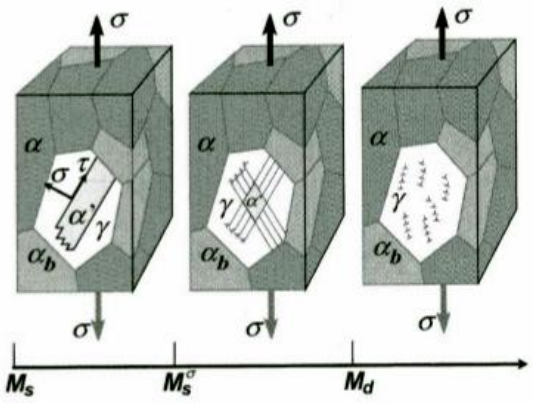

Figure 5: Schematic illustration of dominant deformation mechanism of retained austenite in different temperature ranges in TRIP steel: (from left to right) stress-induced plasticity, strain-induced plasticity and dislocation glide plasticity [23].

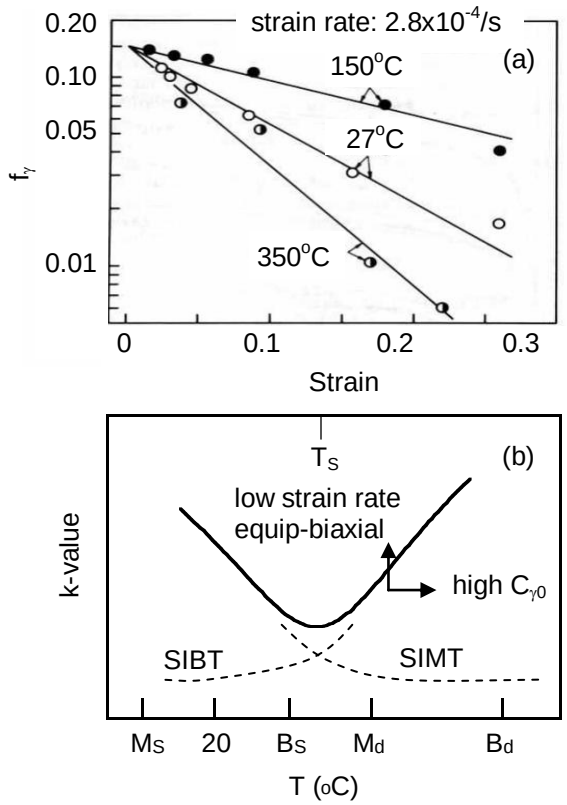

Figure 6 Typical variations in volume fraction of retained austenite (f_γ) as a function of plastic strain (0.4%C-1.5%Si-1.5%Mn TPF steel) [7] and illustration of forming temperature dependence of *k* value of TRIP-aided steel [7,12,36]. SIMT: strain-induced martensite transformation, SIBT: strain-induced bainite transformation.

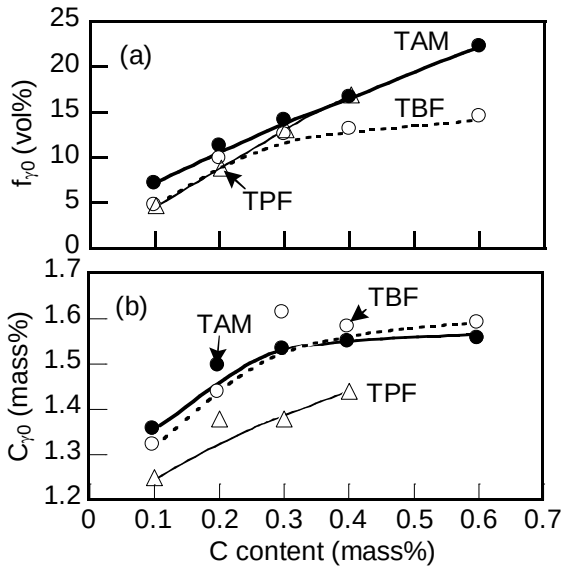

Figure 7: Variations in (a) initial volume fraction ($f_{\gamma 0}$) and (b) initial carbon concentration ($C_{\gamma 0}$) of retained austenite as a function of carbon content in 0.1-0.6%C-1.5%Si-1.5%Mn TRIP-aided steels with different matrix structure [15]. Austempering treatment was conducted at 400^{o}C for 100-3000s.

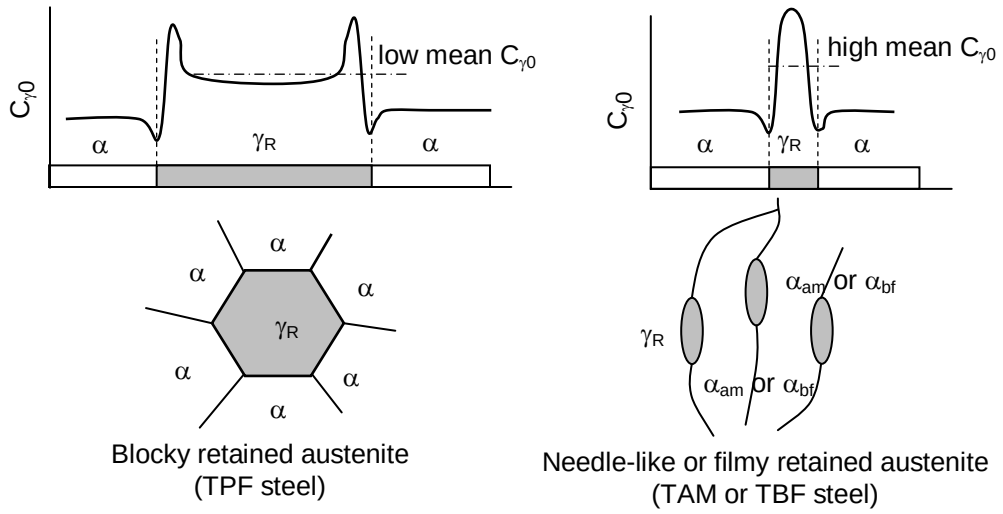

Figure 8: Illustration of carbon concentration distribution in retained austenite of three kinds of TRIP-aided steels.

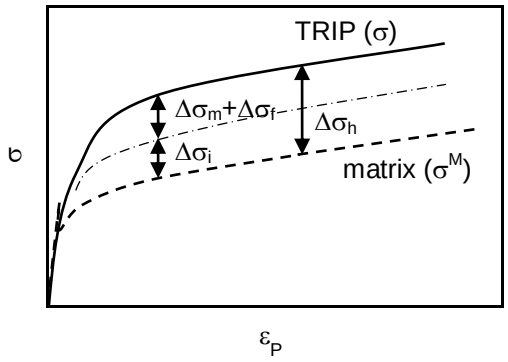

Figure 9: Strain-hardening of TRIP-aided steel.

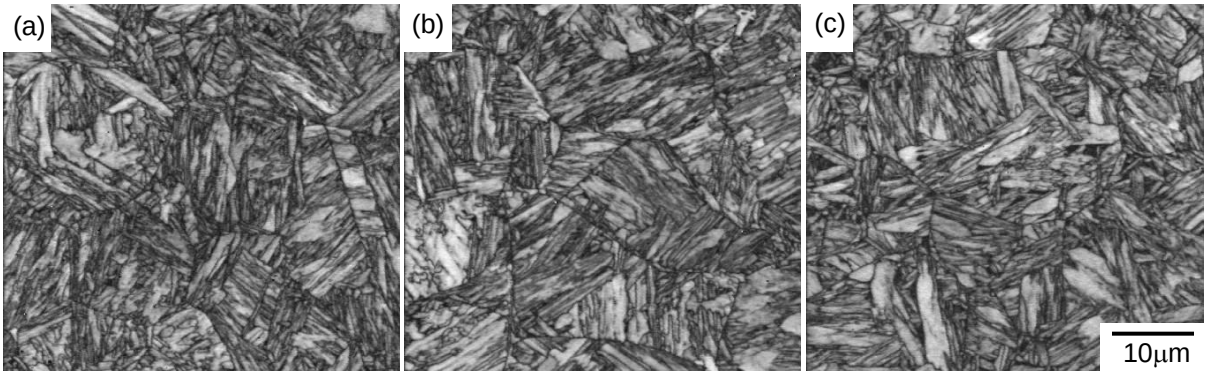

(a) 0.2%C-1.5Si-1.5Mn, $f_{\gamma 0}$=3.4vol%, $C_{\gamma 0}$=1.30mass%
(b) 0.2%C-0.5%Si-1.5%Mn-1.0%Al, $f_{\gamma 0}$=3.6vol%, $C_{\gamma 0}$=1.63mass%
(c) 0.2%C-1.5%Si-2.5%Mn, $f_{\gamma 0}$=5.8vol%, $C_{\gamma 0}$=0.62mass%

Figure 10: Scanning electron micrographs of TBF steels austempered at 325^{o}C, in which $f_{\gamma 0}$ and $C_{\gamma 0}$ are volume fraction and carbon concentration of retained austenite, respectively.

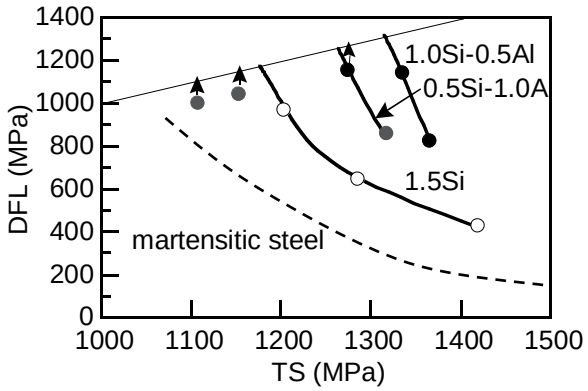

Figure 11: Variation in delayed fracture strength (*DFL*) for 5 hours with tensile strength (*TS*) of 0.20%C-Si-Al-1.55%Mn TBF and 0.40%C-0.16%Si-1.44%Mn martensitic steels.

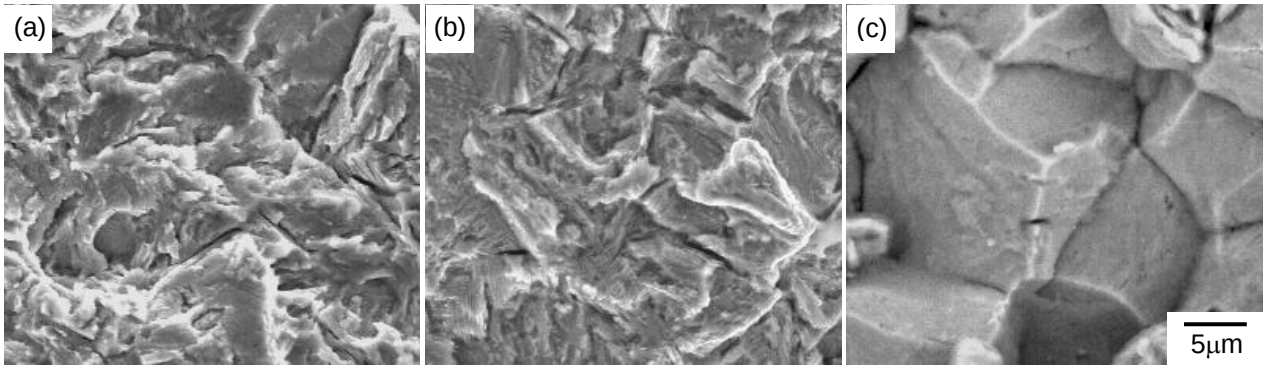

Figure 12: Scanning electron micrographs of delayed fracture surface of TBF steels austempered at 325^{o}C. (a) 0.2%C-1.5Si-1.5Mn, (b) 0.2%C-0.5%Si-1.5%Mn-1.0%Al, (c) 0.2%C-1.5%Si-2.5%Mn.

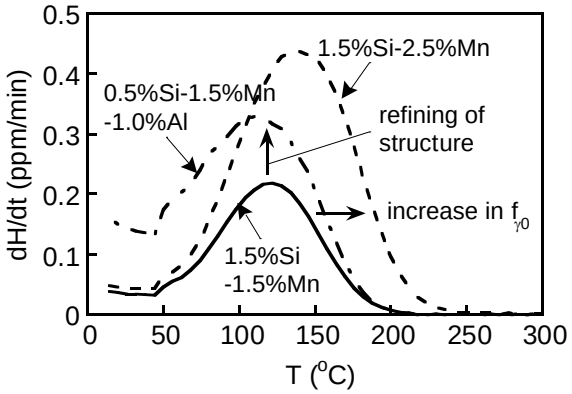

Figure 13: Comparison of hydrogen evolution curve of steels A, D and E austempered at 325°C in 0.2%C-1.5Si-1.5Mn, 0.2%C-0.5%Si-1.5%Mn-1.0%Al and 0.2%C-1.5%Si-2.5%Mn TBF steels. hydrogen charging time: t_C=15min and current density: 500A/m^2.

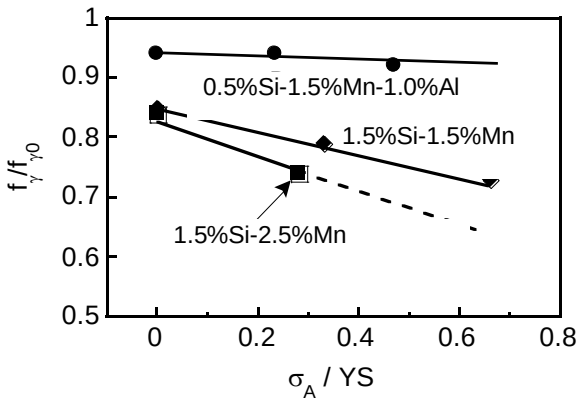

Figure 14: Change in volume fraction (f_γ) of retained austenite as a function of applied stress (σ_A) in 0.2%C-1.5Si-1.5Mn, 0.2%C-0.5%Si-1.5%Mn-1.0%Al and 0.2%C-1.5%Si-2.5%Mn TBF steels. $f_{\gamma 0}$ is initial volume fraction or retained austenite.

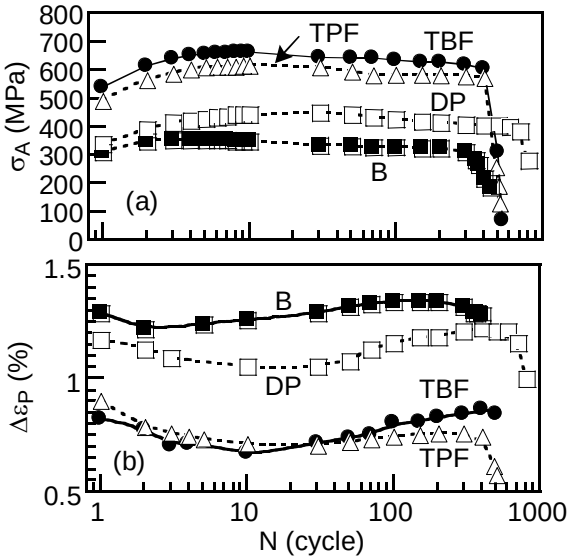

Figure 15: Variations in (a) stress amplitude (σ_A) and (b) plastic strain amplitude (ε_P) with number of cycles (N) for TBF (T_A=450^{o}C), TPF, dual-phase (DP) and bainitic (B) steels.

TBF: 0.17%C-1.41%Si-2.02%Mn, $f_{\gamma 0}$=6.6vol%, $C_{\gamma 0}$=1.20mass%,

TPF: 0.17%C-1.41%Si-2.02%Mn, $f_{\gamma 0}$=11.3vol%, $C_{\gamma 0}$=1.23mass%

DP, B: 0.10%C-0.18%Si-0.43%Mn.

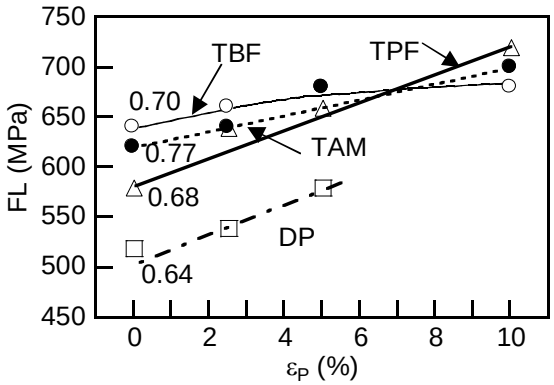

Figure 16: Variations in fatigue limit (*FL*) as a function of prestrain (ε_P) in three kinds of TRIP-aided steels (0.17%C-1.41%Si-2.00%Mn) and dual-phase (DP) steel (0.14%C-0.19%Si-1.69%Mn), in which numerals represent a ratio of fatigue limit to tensile strength of as heat-treated steels. TPF: $f_{\gamma 0}$=8.9vol%, $C_{\gamma 0}$=1.24mass%, TAM: $f_{\gamma 0}$=10.9vol%, $C_{\gamma 0}$=1.31mass%, TBF: $f_{\gamma 0}$=7.5vol%, $C_{\gamma 0}$=1.21mass%.

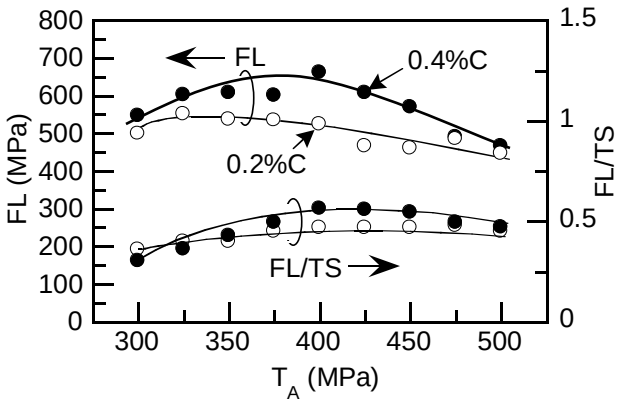

Figure 17: Variations in fatigue limit (*FL*) and a ratio of fatigue limit to tensile strength (*FL/TS*) with austempering temperature (T_A) in 0.2-0.4%C-1.5%Si-1.5%Mn TBF steels austempered at 300-500^{o}C.

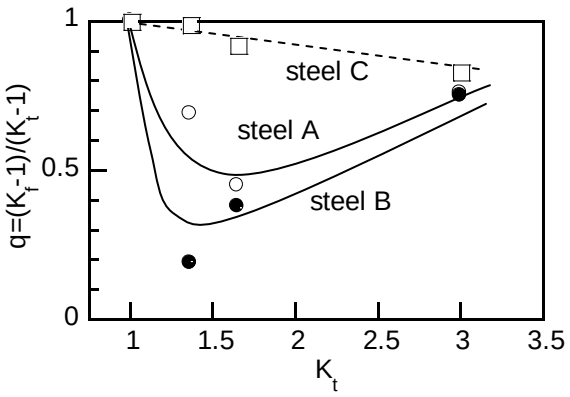

Figure 18: Variations in notch sensitivity index (q) as a function of stress concentration factor (K_t) in TBF steels (steels A and B) and martensitic steel (steel C). This figure is modified from ref. 59.

A: 0.20%C-1.50%Si-1.50%Mn, $f_{\gamma 0}$=7.3vol%, $C_{\gamma 0}$=1.10mass%. B: 0.20%C-0.98%Si-1.48%Mn-0.47%Al-0.05%Nb-0.2%Mo, $f_{\gamma 0}$=7.4vol%,$C_{\gamma 0}$=1.17mass%. C: 0.14%C-0.19%Si-1.69%Mn.

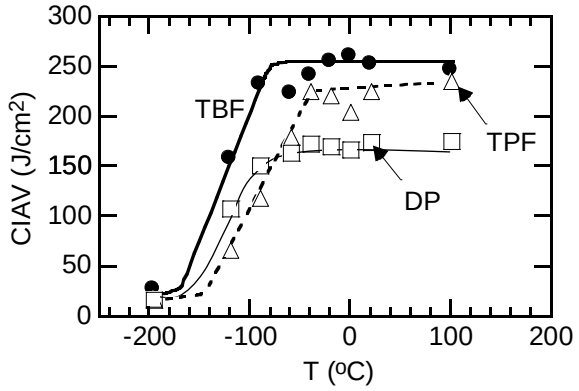

Figure 19: Charpy impact absorbed value (*CIAV*) – testing temperature (*T*) curves of TBF (T_A=375^{o}C), TPF (T_A=400^{o}C) and dual-phase (DP) steels with chemical composition of 0.11%C, 1.3%Si and 1.0%Mn.

TBF: $f_{\gamma 0}$=7.7vol%, $C_{\gamma 0}$=1.48mass%, TPF: $f_{\gamma 0}$=12.8vol%, $C_{\gamma 0}$=1.27mass%.

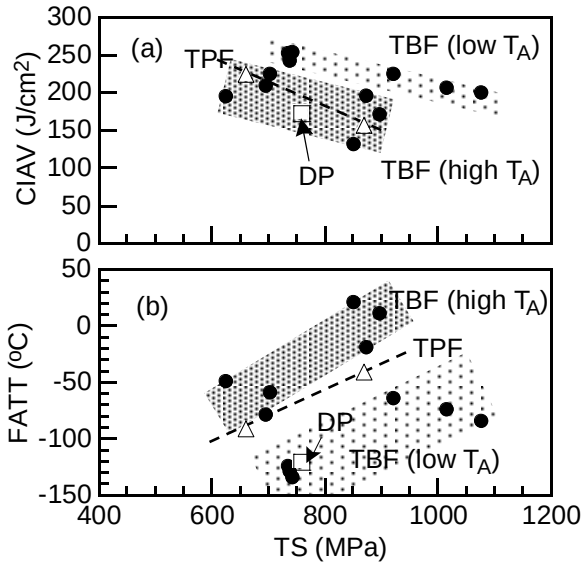

Figure 20: Variations in (a) Charpy impact absorbed value (*SIAV*) at upper shelf region and (b) fracture appearance transition temperature (*FATT*) as a function of tensile strength (*TS*) in TBF, TPF and DP steels. TBF and TPF: 0.11%C-1.3%Si-1.0%Mn, 0.20%C-2.00%Si-1.50%Mn, DP: 0.11%C-1.30%Si-1.00%Mn.

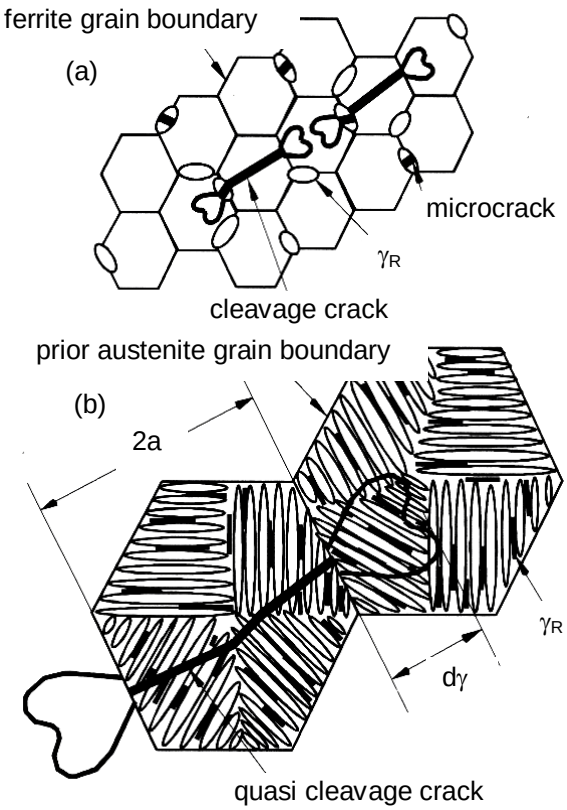

Figure 21: Relationship between plastic zone ($d_Y=K^2/3\pi\sigma_Y^2$) [63] of cleavage or quasi-cleavage crack and mean free path of retained austenite in (a) TPF and (b) TBF steels.

Captions

Figure 1: Typical light micrographs (a-c) and transmission electron micrographs (d, e) of (a) 0.2%C-1.5%Si-1.5%Mn TPF (t_A=1000s), (b, d) TAM (t_A=100s) and (c, e) TBF (t_A=200s) steels austempered at 400^{o}C. In (a)-(c), gray, black and white regions represent matrix ((a) polygonal ferrite, (b) annealed martensite; α_{am}, (c) bainitic ferrite; α_{bf}), cementite-free bainite and retained austenite (γ_R) and/or martensite, respectively.

Figure 2: Development history and comparison of some formabilities of three kinds of low alloy TRIP-aided steels with different matrix structure, polygonal ferrite (TPF), bainitic ferrite (TBF) or annealed martensite (TAM), in which DP and B steels are dual-phase and bainitic steels, respectively.

Figure 3: Annealing-austempering process and pseudo-binary Fe-C-1.5Si-1.5%Mn diagram, in which T_γ and $T_{\alpha+\gamma}$ represent annealing temperatures in γ and $\alpha+\gamma$ regions, respectively. T_A and t_A are austempering temperature and time, respectively.

Figure 4: Relationship between stress-assisted and strain-induced martensite [35]. $\Delta G^{\sigma=0,\ Ms}$ is energy for transformation of austenite to martensite.

Figure 5: Schematic illustration of dominant deformation mechanism of retained austenite in different temperature ranges in TRIP steel: (from left to right) stress-induced plasticity, strain-induced plasticity and dislocation glide plasticity [23].

Figure 6: Typical variations in volume fraction of retained austenite (f_γ) as a function of plastic strain (0.4%C-1.5%Si-1.5%Mn TPF steel) [7] and illustration of forming temperature dependence of k value of TRIP-aided steel [7,12,36]. SIMT: strain-induced martensite transformation, SIBT: strain-induced bainite transformation.

Figure 7: Variations in (a) initial volume fraction ($f_{\gamma 0}$) and (b) initial carbon concentration ($C_{\gamma 0}$) of retained austenite as a function of carbon content in 0.1-0.6%C-1.5%Si-1.5%Mn

TRIP-aided steels with different matrix structure [15]. Austempering treatment was conducted at 400^{o}C for 100-3000s.

Figure 8. Illustration of carbon concentration distribution in retained austenite of three kinds of TRIP-aided steels.

Figure 9: Strain-hardening of TRIP-aided steel.

Figure 10: Scanning electron micrographs of TBF steels austempered at 325^{o}C, in which $f_{\gamma 0}$ and $C_{\gamma 0}$ are volume fraction and carbon concentration of retained austenite, respectively.

Figure 11: Variation in delayed fracture strength (*DFL*) for 5 hours with tensile strength (*TS*) of 0.20%C-Si-Al-1.55%Mn TBF and 0.40%C-0.16%Si-1.44%Mn martensitic steels.

Figure 12: Scanning electron micrographs of delayed fracture surface of TBF steels austempered at 325^{o}C. (a) 0.2%C-1.5Si-1.5Mn, (b) 0.2%C-0.5%Si-1.5%Mn-1.0%Al, (c) 0.2%C-1.5%Si-2.5%Mn.

Figure 13: Comparison of hydrogen evolution curve of steels A, D and E austempered at 325^{o}C in 0.2%C-1.5Si-1.5Mn, 0.2%C-0.5%Si-1.5%Mn-1.0%Al and 0.2%C-1.5%Si-2.5%Mn TBF steels. hydrogen charging time: t_C=15min and current density: 500A/m^2.

Figure 14: Change in volume fraction (f_{γ}) of retained austenite as a function of applied stress (σ_A) in 0.2%C-1.5Si-1.5Mn, 0.2%C-0.5%Si-1.5%Mn-1.0%Al and 0.2%C-1.5%Si-2.5%Mn TBF steels. $f_{\gamma 0}$ is initial volume fraction or retained austenite.

Figure 15: Variations in (a) stress amplitude (σ_A) and (b) plastic strain amplitude (ε_P) with number of cycles (*N*) for TBF (T_A=450^{o}C), TPF, dual-phase (DP) and bainitic (B) steels.
TBF: 0.17%C-1.41%Si-2.02%Mn, $f_{\gamma 0}$=6.6vol%, $C_{\gamma 0}$=1.20mass%,

TPF: 0.17%C-1.41%Si-2.02%Mn, $f_{\gamma 0}$=11.3vol%, $C_{\gamma 0}$=1.23mass%
DP, B: 0.10%C-0.18%Si-0.43%Mn.

Figure 16: Variations in fatigue limit (*FL*) as a function of prestrain (ε_P) in three kinds of TRIP-aided steels (0.17%C-1.41%Si-2.00%Mn) and dual-phase (DP) steel (0.14%C-0.19%Si-1.69%Mn), in which numerals represent a ratio of fatigue limit to tensile strength of as heat-treated steels. TPF: $f_{\gamma 0}$=8.9vol%, $C_{\gamma 0}$=1.24mass%, TAM: $f_{\gamma 0}$=10.9vol%, $C_{\gamma 0}$=1.31mass%, TBF: $f_{\gamma 0}$=7.5vol%, $C_{\gamma 0}$=1.21mass%.

Figure 17: Variations in fatigue limit (*FL*) and a ratio of fatigue limit to tensile strength (*FL/TS*) with austempering temperature (T_A) in 0.2-0.4%C-1.5%Si-1.5%Mn TBF steels austempered at 300-500^{o}C.

Figure 18: Variations in notch sensitivity index (q) as a function of stress concentration factor (K_t) in TBF steels (steels A and B) and martensitic steel (steel C). This figure is modified from ref. 59.
A: 0.20%C-1.50%Si-1.50%Mn, $f_{\gamma 0}$=7.3vol%, $C_{\gamma 0}$=1.10mass%.
B: 0.20%C-0.98%Si-1.48%Mn-0.47%Al-0.05%Nb-0.2%Mo, $f_{\gamma 0}$=7.4vol%,$C_{\gamma 0}$=1.17mass%.
C: 0.14%C-0.19%Si-1.69%Mn.

Figure 19: Charpy impact absorbed value (*CIAV*) – testing temperature (*T*) curves of TBF (T_A=375^{o}C), TPF (T_A=400^{o}C) and dual-phase (DP) steels with chemical composition of 0.11%C, 1.3%Si and 1.0%Mn.
TBF: $f_{\gamma 0}$=7.7vol%, $C_{\gamma 0}$=1.48mass%, TPF: $f_{\gamma 0}$=12.8vol%, $C_{\gamma 0}$=1.27mass%.

Figure 20: Variations in (a) Charpy impact absorbed value (*SIAV*) at upper shelf region and (b) fracture appearance transition temperature (*FATT*) as a function of tensile strength (*TS*) in TBF, TPF and DP steels. TBF and TPF: 0.11%C-1.3%Si-1.0%Mn, 0.20%C-2.00%Si-1.50%Mn, DP: 0.11%C-1.30%Si-1.00%Mn.

Figure 21: Relationship between plastic zone ($d_Y=K^2/3\pi\sigma_Y^2$) [63] of cleavage or quasi-cleavage crack and mean free path of retained austenite in (a) TPF and (b) TBF steels.